Efficient heat transfer in a regime of elastic turbulence

Boubou Traore, Cathy Castelain, Teodor Burghelea

Efficient heat transfer in a regime of elastic turbulence

Boubou Traore, Cathy Castelain, Teodor Burghelea

LUNAM Université, Université de Nantes, CNRS, Laboratoire de Thermocinétique, UMR 6607, La Chantrerie, Rue Christian Pauc, B.P. 50609, F-44306 Nantes Cedex 3, France

Abstract

By systematic measurements of the statistics of temperature fluctuations at various positions within a viscoelastic von Karman flow cooled from below it is found that within an elastic turbulent flow regime the heat transfer efficiency may locally increase up to 4 times which is comparable to the efficiency increase observed in the case of inertial turbulence at $Re \approx 1600$. In spite of the inhomogeneous rheological properties induced by the temperature gradient, several similarities with the decay of a low diffusivity tracer in a random smooth flow (Batchelor regime) are found: exponential tails of the probability distribution functions, algebraic decay of the power spectra, $P \propto f^{-\beta}$ with $\beta \approx -1.1$, exponential decay of the second order moment of the fluctuations. The similarity with the passive scalar decay passive problem is reinforced by a comparative analysis of the isothermal and non-isothermal flow patterns which reveals no significant effect of the heat transfer process on the flow topology.

Keywords: elastic turbulence, heat transfer, intermittency,

Email addresses: Cathy.Castelain@univ-nantes.fr (Cathy Castelain), Teodor.Burghelea@univ-nantes.fr (Teodor Burghelea)

Contents

List of Figures

1. Introduction

The efficient transport of mass and heat within fluids is of paramount importance in many industrial settings such as the development of efficient heat exchangers, cooling the magnetic coils of particle accelerators and the central processing units (CPU's) of personal computers. The natural mechanisms by which the mass and the heat are transported within a fluid are the molecular diffusion and the thermal conduction, respectively. These mechanisms, however, are the least efficient ones in the sense that the characteristic times over which they take place are significantly large.

An increase in the efficiency of the mass and heat transport can be obtained by generating flows with divergent Lagrangian trajectories which are able to efficiently stretch, fold and breakup the fluid elements down to sufficiently small spatial scales when the molecular diffusion and the thermal conduction can effectively homogenise the mass/temperatures distributions.

One way of generating random fluid motion is to trigger inertial turbulent flow states by ensuring sufficiently large values of the Reynolds number $Re = \rho UL/\eta$. Here ρ stands for the density of the fluid, L for the characteristic size of the flow container, U for the scale of the fluid velocity and η for the viscosity of the fluid. It has been demonstrated that inertial turbulent flows transport efficiently both mass and heat [14, 24, 41, 35, 25, 22].

There exist, however, various practical situations when increasing the Reynolds number is a difficult task, particularly when the characteristic size of the fluid container L is small, e.g. in a micro channel. In such situations, it is desirable to replace the inertial nonlinearity in the momentum equation with other types of nonlinearities.

Exponentially divergent Lagrangian fluid trajectories can be generated by the laminar chaotic advection [1, 31] and, consequently, such flows are able to efficiently transport both mass and heat within a fluid, [39, 40, 21, 13, 29, 30]. Triggering the laminar chaotic advection at moderate Re requires, however, a special design of the flow channel and/or a particular flow control, e.g. controlled pulsations [36]. This can also become quite challenging in the case of microscopic flows.

The basic hydrodynamic stability picture of flows of Newtonian fluids can be drastically changed by a small addition of flexible, high molecular weight linear polymers [3]. Solutions of those polymers are known as non-Newtonian viscoelastic fluids [3]. The mechanical stresses within these fluids are history dependent with some characteristic relaxation time, λ, which in the case of dilute solutions is a time of relaxation of individual polymer molecules.

Another specific property of the polymer solutions is the nonlinear dependence of the polymer contribution to the stress on the rate of deformation in the flow, ∇V, [3]. This nonlinearity usually becomes significant when the Weissenberg number, $Wi = \lambda \nabla V$, becomes on the order of unity. The latter plays a similar role to the Reynolds number in the sense that it reflects the competition between (elastic) nonlinearity and dissipation. The nonlinear growth of the elastic polymer stresses is especially striking during uniaxial extensional flows at $Wi > 1/2$, where the apparent extensional viscosity of polymer solutions can increase by up to three orders of magnitude as the total deformation increases [37].

The non-linear polymer stresses in curvilinear shear flows can also lead to elastic turbulence, a random multiscale three-dimensional flow, which can develop at arbitrarily low Re [15] and evolves independently on it.

Several subsequent experimental studies of flows in a regime of elastic turbulence have revealed a number of fundamental features of this phenomenon.

The transition to the elastic turbulence is accompanied by a sharp growth of the flow resistance [15, 17].

The elastic turbulent flows exhibit divergent Lagrangian trajectories and, consequently, positive finite time Lyapunov exponents (**FTLE**) could be measured by both numerical integration of the measured velocity fields and by direct tracking of tracer particles in the flow, [7].

Within a regime of elastic turbulence, the flow fields are spatially smooth and characterised by a single scale set by the size of the fluid container L, [9, 4, 8].

The elastic turbulence was found to mix efficiently viscous streams in both curvilinear macro-channels [16, 23] and curvilinear micro channels [5, 6]. A systematic analysis of the statistical properties of the decay regime of mixing has demonstrated that the elastic turbulent flow in a curvilinear open channel is an ideal realisation of the so called Batchelor regime of mixing, [6]. Whereas the ability of elastic turbulent flows to mix low diffusivity passive tracers has been demonstrated experimentally and the statistical and scaling properties of the decay regime of mixing have been systematically investigated, [23], there exist practically no experimental studies on the efficiency of the heat transfer within an elastic turbulent flow.

The temperature field advected by a random flow field may act either as a passive scalar (*i.e.* which does not locally modify the flow field) in the absence of buoyancy forces or as an active one when buoyancy forces are present, [10].

In the case of a random flow of a dilute polymer solution in a regime of elastic turbulence the similarity between the heat transfer process and the mixing of a passive scalar previously investigated is not granted even in the absence of buoyancy. This is because local changes of the temperature within the flow of the polymer solution usually trigger changes of the polymer relaxation time and consequently of the polymer contribution to the stress tensor which could locally modify the flow field. Thus, the heat transport by elastic turbulence deserves a separate study.

We report in this paper a first (to our best knowledge) experimental study of the heat transport within the von Karman flow of a dilute solution of high molecular weight flexible and linear polymers in a regime of elastic turbulence. The motivation of choosing this flow configuration for a first experimental study is two fold. First, there exists a significant number of experimental studies referenced above that systematically characterise (in both space and time domains) the main features of elastic turbulent flows in this geometry. Second, this macroscopic flow configuration allows an easier instrumentation for the characterisation of the heat transfer process as well for the characterisation of the flow fields.

The paper is organised as follows. The experimental apparatus and the measuring techniques are described in Sec. 2.1. The choice, the preparation and the physical characterisation of the polymer solution are detailed in Sec. 2.2.

The experimental results are presented in Sec. 3. The transition to the elastic turbulence and the main features of the turbulent flow are discussed in Sec. 3.1. A quantitative assessment of the local intensity of the heat transfer process as well as a statistical characterisation of the temperature fluctuations in a regime of elastic turbulence are presented in Sec. 3.3.

The paper closes with a summary of the main findings, Sec. 4.

2. Experiment

2.1. Experimental apparatus and measuring techniques

The experimental setup is schematically illustrated in Fig. 1. It consists of an acrylic made fluid container **FC** with the radius $R_c = 40$ *mm* and optically transparent walls. The flow is driven by a rotating top disk **D** with a radius $R_d = 39$ *mm* mounted on the shaft of a commercial rheometer, Mars III (from Thermofischer). The use of the commercial rheometer in driving the flow is justified by the accurate control of both the rotation speed Ω and the driving torque M. The distance between the top disk and the bottom of the fluid container was $H = 60$ *mm* for all the experiments reported in the paper.

The temperature of the bottom of the fluid container is controlled via a circulating fluid bath **CFB** fed with deionised water by a thermally stabilised fluid circulator (Lauda, model Proline RP 855). To avoid triggering the thermal convection, the temperature within the circulating fluid bath **CFB** is set to $T_b = 13^oC$ which is smaller than the room temperature $T_0 = 23^oC$. To ensure a good repeatability and reproducibility of the experiments, the room temperature has been regulated (with an accuracy of $\pm 0.5^oC$) at all times and for each of the experiments reported herein by an air conditioning system installed in the experimental room.

The distribution of the temperature into the flow is point-wise monitored by an array of six thermocouples T_{1-6} (Chromel-Alumel, 100 μm in size) disposed equidistantly along the vertical direction z and positioned at the radial position $r = R_c/2$, Fig. 1. The thermocouples are mounted through thin metal tubes which allows one to scan the temperature distribution along the radial direction. The signals of the thermocouples are passed to the digitising block $\mathbf{A_2D}$ via the reference box **RB**. The subtraction of the reference temperature by the reference box **RB** diminishes the instrumental error of the temperature readings down to roughly 0.5% of the measured value.

Together with the point-wise measurements of the temperature, the flow has been investigated by local measurements of the flow fields by the Digital Partical Image Velocimetry (**DPIV**) technique. For this purpose, a green laser beam ($\lambda = 514nm$) with a power of 500 mW emitted by the solid state laser **L** (from Changchun Industries, Model LD-WL206) is deflected by a system of planar mirrors to a cylindrical optics block **CO** which reshapes it in a horizontal laser sheet **LS**, Fig. 1. The cylindrical optics block is composed of a glass rod with a short focal distance $f_1 = 2$ *mm* and a cylindrical lens with a larger focal distance, $f_2 = 7cm$. The two optical elements are mounted orthogonally to each other and in a telescopic arrangement such as the primary horizontal laser sheet generated by the glass rod is

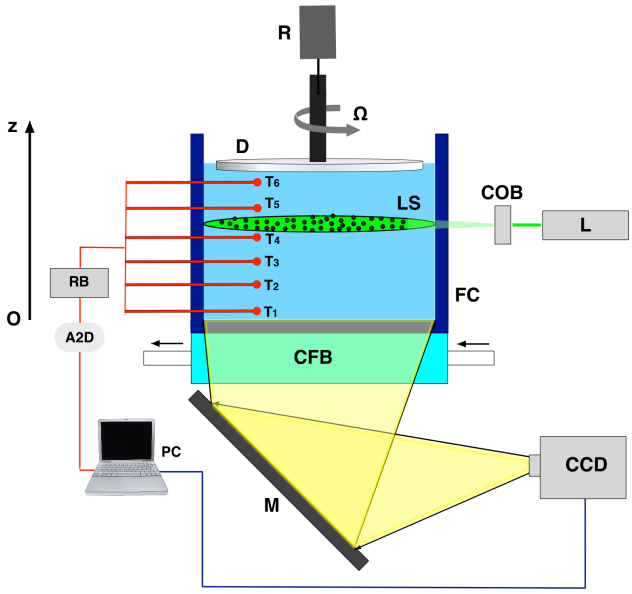

Figure 1: Schematic view of the experimental setup: **R** - the shaft of the rheometer, **D** - rotating disk, **FC** - fluid container, **CFB** - circulating fluid bath, $\mathbf{T_{1-6}}$ - thermocouples, **RB** - reference box, $\mathbf{A_2D}$ - analogue to digital converter , **L** - solid state laser, **LS** - laser sheet, **COB** - cylindrical optics block, **M** - planar mirror, **CCD** - video camera, **PC** - personal computer.

focused on the vertical direction in the middle of the flow channel by the second lens minimising thus its thickness in the measurement region. The thickness of the generated laser sheet is roughly $80\mu m$ in the beam waist region which is positioned at the centre of the fluid container **FC**. The horizontal laser sheet has been positioned in the vicinity of the thermocouple T_4, Fig. 1. The working fluid was seeded with an amount of 200 parts per million (ppm) of polyamide particles with a diameter of $20\mu m$ (from Dantec Dynamics).

Time series of the velocity fields were obtained by a iterative multi-grid **DPIV** algorithm implemented in house under Matlab [32, 34]. For this purpose, a sequence of flow images has been acquired with a colour **CCD** camera which visualises the illuminated flow section through the planar mirror **M**. The total image acquisition time was one minute within the laminar regime and five minutes within the transitional and fully developed elastic turbulent regimes which allowed one to properly capture the flow de-correlation beyond the onset of the primary elastic instability. The inter-frame has been adapted to the measured flow speed in order to maintain the average displacement of the tracer particles in the optimal range of $5-15$ pixels. Together with this, the size of the smallest interrogation window has been adapted to the mean flow velocity corresponding to the value angular speed of the top rotating disk **D** which sets a scale for the mean displacement of the flow tracers in the field of view. The spatial resolution of the measured flow fields was 3 mm. Using this adaptive **DPIV** protocol the instrumental error of the measured velocity fields does not exceed 7% through all the experiments reported herein.

2.2. Choice, preparation, thermal and thermorheological characterisation of the working fluid

A 100 parts per million (ppm) polyacrylamide (**PAAM**) solution with the molecular weight $M_w = 18 \cdot 10^6$ Da has been used as a working fluid. The solvent was a 65% aqueous solution of sucrose. The viscosity of the Newtonian solvent was $\eta_s = 114$ $mPas$ (at the room temperature T_0) which ensures large characteristic relaxation times of the polymer solution.

The polymer solutions were prepared according to the following protocol. First we dissolved $0.9g$ of anhydrous **PAAM** and 3 g of $NaCl$ into 275 ml of de-ionised water by gentle shaking. $NaCl$ was added to fix the ionic contents within the polymer solution. Next the solution was mixed for 3 h in a commercial mixer with a propeller at a moderate speed. The rationale for this step is to cause a controlled mechanical degradation of the longest **PAAM** molecules, in order to cut the tail of the molecular weight distribution of the broadly dispersed **PAAM** sample. In a solution with a broad distribution of polymer molecular weights, the heaviest molecules, which are most vulnerable to mechanical

degradation, bring the major contribution to the solution elasticity, but may break in the course of the experiment. This can lead to inconsistency of the experimental results. We found empirically that the procedure of pre-degradation in the mixer leads to substantial reduction of degradation during the experiments and to substantial improvement of their consistency. Finally, $9g$ of isopropanol was added to the solution to preserve it from ageing and water was added up to $300g$. The final concentrations of **PAAM**, $NaCl$, and isopropanol in the stock solution were 3000 ppm, 1%, and 3%, respectively. This master solution was used to prepare 100 ppm **PAAM** solution in a Newtonian solvent.

The density of the solution was measured at room temperature by weighting fixed volumes of fluid, $\rho = 1200\, kgm^{-3}$.

The thermal properties of the polymer solution have been investigated using a hot disk thermal conductivity analyser (C- Therm, model TC_5). The thermal diffusivity coefficient was measured $\kappa = 1.31 \cdot 10^{-7} m^2\ s^{-1}$ and the characteristic time associated to the thermal diffusion may be estimated as $t_d = H^2/\kappa \approx 25714\ s$. We also note that within the temperature range explored through our experiments no significant temperature dependence of thermal diffusivity coefficient was observed.

The rheological properties of the solvent and of the polymer solution were measured with the same Mars III rheometer around which the complete experimental setup was built. The shear viscosity of the solution was measured with a cone and plate geometry ($D = 60\ mm$, $2\ deg$ truncation) via a controlled rate flow ramp at three temperatures which are relevant during the heat transfer process, $T = 17^oC,\ 19^oC,\ 21^oC$. Corresponding to each value of the imposed rate of shear the stress was allowed to equilibrate during 50 s and the averaging was performed during the last 10 s. The choice of this temperature range was based on the value of the room temperature and of the thermal equilibrium temperature achieved during our experiments, $T_e \approx 16.9^oC$. The temperature was controlled during the rheological measurements by a Peltier system. The geometry has been enclosed by a teflon made solvent trap in order to minimise the sample evaporation and insure the reliability of the measurements. For each temperature, the viscosity measurement has been repeated three times with a freshly loaded sample in order to check the reliability and specify an error bar.

The results of the shear viscosity measurements performed in a range of shear rates and temperatures relevant to the heat transport experiments are presented in Fig. 2(a).

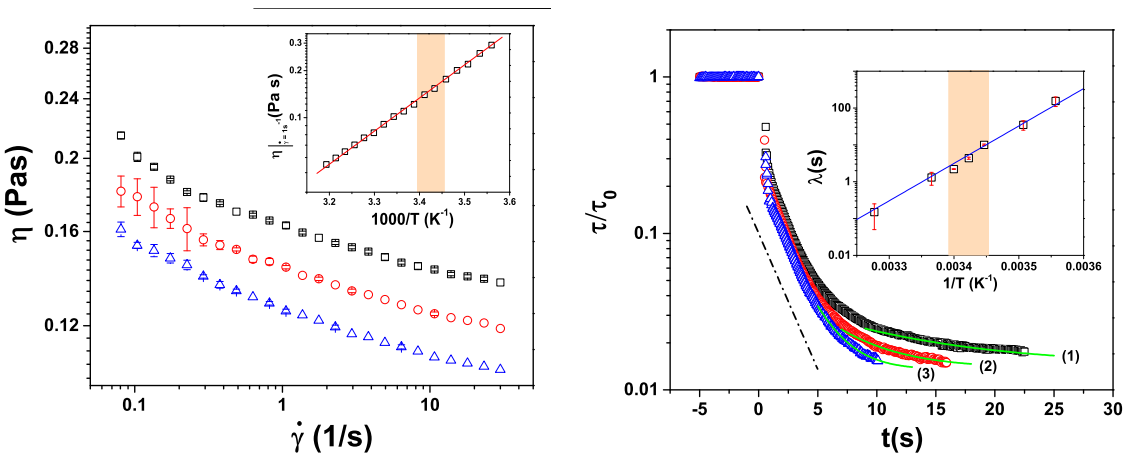

(a) (b)

Figure 2: (a) Flow curves measured during controlled rate flow ramps. The insert presents the temperature dependence of the viscosity measured at $\dot{\gamma} = 1s^{-1}$ and the full line is an Arrhenius fit. (b) Stress relaxation data. The full lines are exponentially decaying functions characterising the slow relaxation mode. The dash-dot line is a guide for the eye, $\tau/\tau_0 \propto e^{-t/2.6(\pm 0.2)}$, highlighting the fast decay mode. The temperature dependence of the longest relaxation time is presented in the insert. The error bars are defined via the nonlinear fitting error. In each panel, the symbols refer to different operating temperatures: squares (□) - $T = 17^oC$, circles (○) -$T = 19^oC$, triangles (△) -$T = 21^oC$.

The viscosity follows an Arrhenius time dependence on the temperature (see the full line in the insert of Fig. 2(a)), $\eta \propto e^{\frac{E_a^\eta}{RT}}$, where R is the ideal gas constant. The viscosity activation energy is found $E_a^\eta \approx 40.625(\pm 1.2) kJ/(mol\ K)$.

The largest polymer relaxation time has been assessed using the stress relaxation method, [26, 27]. For this purpose, a constant rate of shear $\dot{\gamma} = 1s^{-1}$ has been maintained for 50 s. At the time instant $t_0 = 0$ the rate of shear has

been set to 0 and the time decay of the stress has been monitored. As compared to the small amplitude oscillatory measurements, the relaxation time assessed via this technique is independent on the value of the initial shear (if the initial shear rate is sufficiently small so the inertial effects associated to both the shaft of the rheometer and the measuring geometry don't play a significant role), [26]. In addition to that, the largest relaxation time obtained via this method is directly comparable to the relaxation time measured via the relaxation of single molecules observed via fluorescent microscopy, [26]. Relaxation measurements performed at the same temperatures as the shear measurements are illustrated in Fig. 2(b). At each temperature a two mode exponential decay is observed. The fast mode highlighted by the dash-dotted line has a characteristic time $\lambda_1 = 2.6\ s(\pm 0.2\ s)$ which is independent on the operating temperature. The largest relaxation time λ associated to the slow mode (see the full lines in Fig. 2(b)) depends on the temperature according to an Arrhenius type law $\lambda \propto e^{\frac{E_a^\lambda}{RT}}$, the insert in Fig. 2(b). Although it is commonly believed that the viscosity activation energy should be close to the relaxation time activation energy, we obtain a significantly larger value, $E_a^\lambda \approx 193.5(\pm 4) kJ/(mol\ K)$. A possible explanation for this rather unexpected result is that the changes of the relaxation time with the temperature for this polymer solution are triggered not only by the changes of the solvent viscosity but some other changes in the molecular properties of the polymer chains.

By taking into account the shear thinning of the viscosity illustrated in Fig. 2(a), the Reynolds number was calculated according to $Re = \frac{\Omega R_i^2 \rho}{\eta(\dot{\gamma})}$ where Ω is the angular speed of the top driving disk **D**. Corresponding to the largest value of Wi we have explored and considering an average value of the shear viscosity within the relevant temperature range, we have found $Re \approx 26$.

The main conclusion of the thermorheological analysis presented above is that in spite of a rather limited temperature range non-negligible changes in both the shear viscosity and the largest polymer relaxation time are observed. Thus, even in the absence of a buoyancy term in the momentum equation (in which case the temperature acts as an *active* scalar field), one can not a priori establish a similarity between the dynamics of a *passive* scalar in a random smooth flow and the transport of heat by elastic turbulence. This further reinforces the motivation of our study.

The Prandtl number $Pr = \frac{\eta(\dot{\gamma})}{\rho \kappa}$ which quantifies the balance between the viscous momentum diffusion and the thermal diffusion varied during our experiments (because of the shear thinning behaviour of the viscosity and its T dependence) in the range $Pr \in [744; 1336]$.

3. Results

3.1. Observation and characterisation of elastic turbulent flow states

We focus in the following on a brief characterisation of the transition to elastic turbulence and its main flow features in isothermal conditions at the room temperature T_0.

At an integral scale, the transition to elastic turbulence via a primary elastic instability can be monitored by measurements of the statistics power P injected into the flow as a function of the Weissenberg number. The injected power is calculated for the case of a swirling flow as $P = M \cdot \Omega$ where M is the torque acting on the shaft of the rheometer.

The statistics of the injected power have been quantified by performing a controlled rate flow ramp. For each value of the imposed angular speed Ω of the top disk **D** we have collected time series of the torque $M(t)$ and finally calculated the time averaged injected power as $\bar{P} = \langle P(t) \rangle_t$ and the root mean square (rms) of the power fluctuations as $P^{rms} = \left\langle (P(t) - \bar{P})^2 \right\rangle_t^{1/2}$. The statistics has been carried on over a time interval $\Delta t = 40\ s$.

First, we illustrate such measurements for the case when the sucrose solvent was used and the angular speed was varied over the entire range of Reynolds numbers explored with the polymer solution, Fig. 3. Within the entire range of angular speeds (Re) the time averaged power scales quadratically with the angular speed (the full line in Fig. 3) consistently with a linear relationship between the torque and the angular speed. Second, we note that the fluctuations of the power quantified by the ratio $P^{rms}/\bar{P}$ do not exceed 3% of the mean value.

On the other hand it is known that the inertially turbulent von Karman flow of a Newtonian fluid is characterised by strong (typically larger than 15% of the mean) strongly non Gaussian fluctuations of the injected power and a cubic scaling of the mean power with the angular speed, [38].

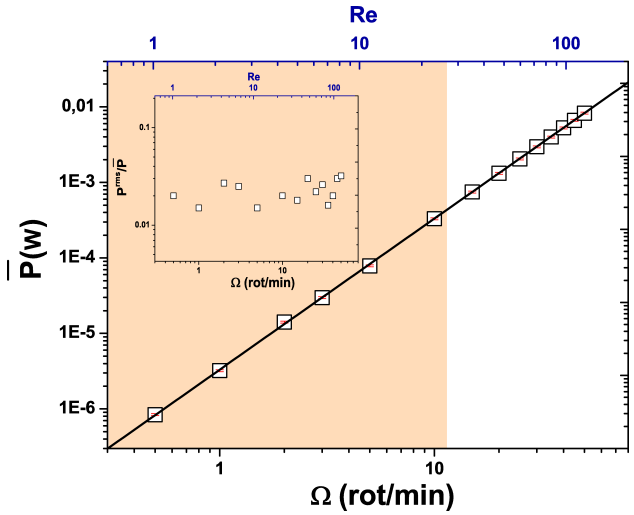

Figure 3: Dependence of the time averaged injected power $\bar{P}$ measured with the solvent alone at the room temperature T_0 on the angular speed Ω of the top disk. The corresponding values of the Reynolds number are shown on the top horizontal axis. The full line is a quadratic fit $\bar{P} = (3.3 \cdot 10^{-6} \pm 1.5 \cdot 10^{-8})\Omega^2$. The highlighted region corresponds to the range of Re explored during the experiments with the polymer solution. The reduced power fluctuations are presented in the insert.

We can therefore conclude that within the range of Re explored during the measurements performed with the polymer solution no inertial instability is expected to occur and thus all the flow and heat transfer characteristics we present in the following should be solely attributed to the elastic contribution of the polymer molecules to the stress.

The statistics of the power fluctuations measured with the polymer solution as a function of the Weissenberg number is illustrated in Fig. 4. The Weissenberg number was calculated as $Wi = \dot{\gamma} \cdot \lambda$. Based on the measurements presented in Fig. 2(b), we have chosen $\lambda = 5.5\ s$ which is the average value within the temperature interval considered.

Corresponding to a a critical value of the Weissenberg number $Wi_c \approx 2$, an increase of the flow resistance is observed in the form of an increase of the averaged injected power beyond its laminar value $\bar{P}_{lam}$, Fig. 4(a). This corresponds to a primary elastic instability that occurs in the flow. Simultaneously with this, an increase of the rms of the power fluctuations is observed, Fig. 4(b). The experimentally determined scaling laws of both the flow resistance $\bar{P}/\bar{P}_{lam} \propto Wi^{0.67}$ and of the reduced rms of the fluctuations, $P^{rms}/P^{rms}_{lam} \propto Wi^3$, are consistent with previous measurements, [9, 4].

The evolution of the flow structure with the Weissenberg number is illustrated in Fig. 5. The **DPIV** measurements are performed in an horizontal plane located in the vicinity of the thermocouple T_4 at $z \approx H/2$ (Fig. 1). The top row of Fig. 5 presents the flow fields averaged over times typically 10 times larger than the polymer relaxation time λ and the bottom row presents the time averaged in plane vorticity $\langle \omega_z \rangle_t$.

The flow field measured below the onset of the primary elastic instability at $Wi = 0.8$ is dominated by a stationary and off-centred Ekman vortex, [12]. This flow structure is different from that of the laminar flow observed in Ref. [9] (see Fig. 10(a) therein) which was consistent with a rigid body rotation around the symmetry axis of the fluid container **FC** and had no vertical velocity component.

This difference can be explained by the presence of the array of thermocouples which perturb the base flow, see Fig. 1. The off-centred flow topology observed in the laminar regime is consistent with the presence of a steady vertical flow component which may slightly enhance the heat transfer (as compared to the purely conductive state) even below the onset of the elastic instability. The effect of the thermocouples on the laminar flow can also be noticed in the map of the time averaged vorticity presented on the second row of Fig. 5.

The topology of the mean flow and vorticity field changes as one moves towards the transitional ($Wi = 7.7$) and fully developed elastic turbulent ($Wi = 15.4$) flow regimes.

Within the transitional regime, the flow is dominated by an unsteady toroidal vortex. Within the elastic turbulent regime, the flow topology changes to a randomly fluctuating spiral vortex, in agreement with the previous results on the elastic turbulence in von Karman flows, [9, 4]. Within the elastic turbulent regime the flow is spatially smooth,

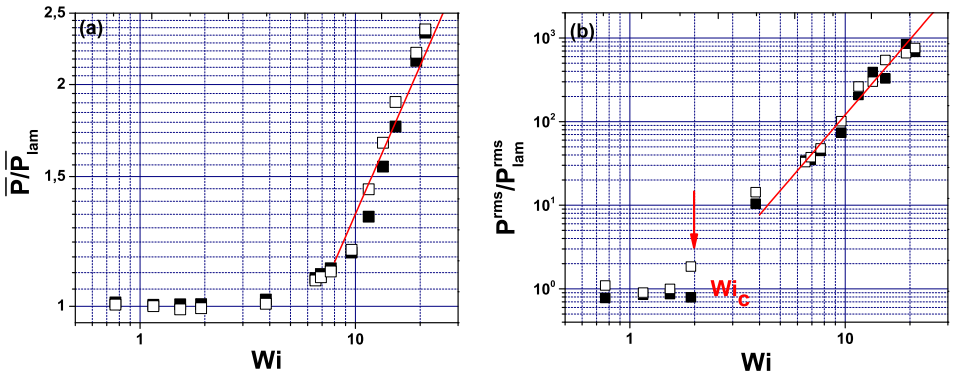

Figure 4: **(a)** Dependence of the normalised time averaged injected power $\bar{P}/\bar{P}_{lam}$ on the Weissenberg number Wi. The full line is a guide for the eye, $\bar{P}/\bar{P}_{lam} \propto Wi^{0.67}$. **(b)** Dependence of the reduced rms of the power fluctuations P^{rms}/P^{rms}_{lam} on the Weissenberg number Wi. The full line is a guide for the eye, $P^{rms}/P^{rms}_{lam} \propto Wi^3$. The full/empty symbols refer to increasing/decreasing Wi. The vertical arrow indicates the onset of the primary elastic instability Wi_c.

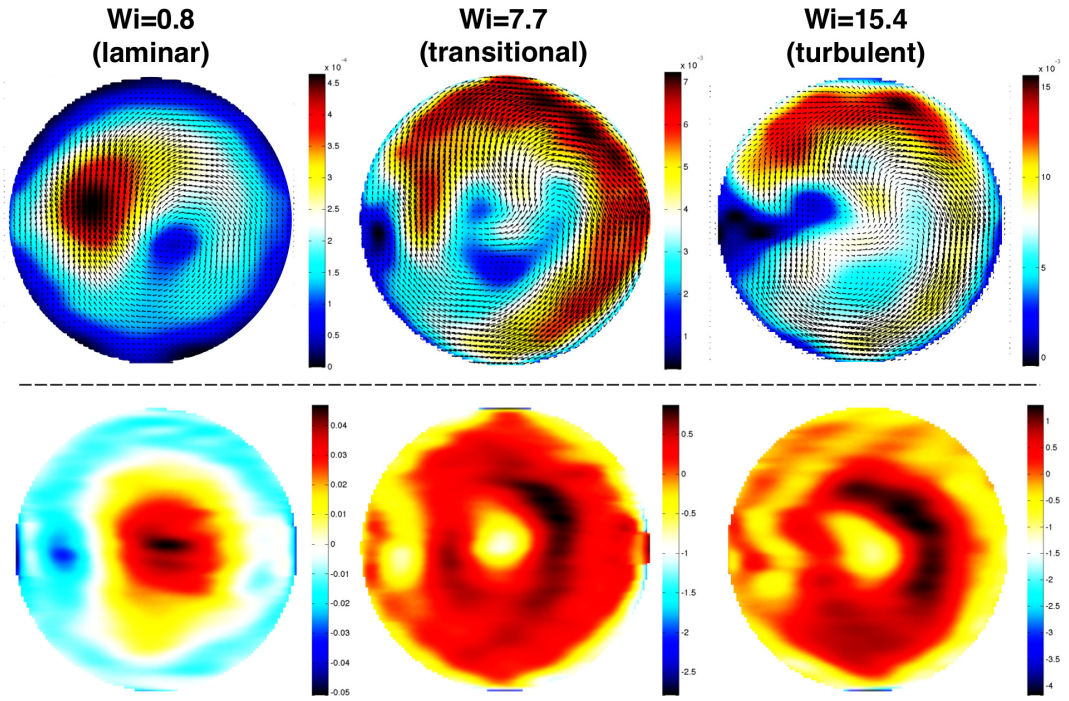

Figure 5: Top row: time averaged flow patterns for various Weissenberg numbers indicated in the top inserts. The colour map refers to the modulus of the in-plane velocity. For the clarity of the presentation, the overlapped vector fields were down-sampled by a factor of 2 along each direction. Bottom row: time averaged vorticity, $\langle \omega_z \rangle_t$. The measurements were performed in isothermal conditions at the room temperature T_0.

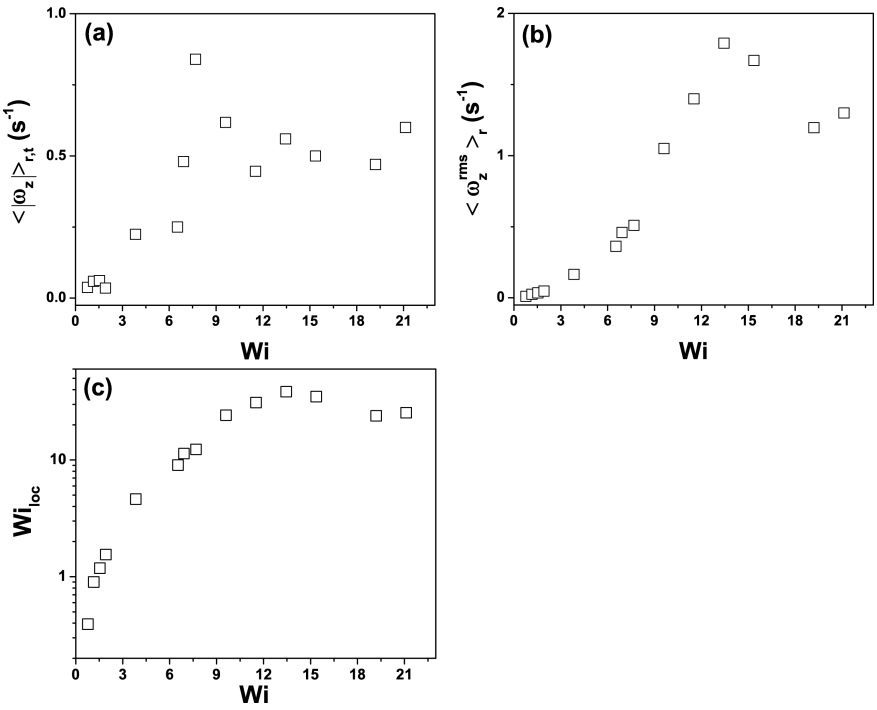

Figure 6: **(a)** Dependence of the modulus of the vorticity averaged over the entire field of view and over several minutes $\langle|\omega_z|\rangle_{r,t}$ on the Weissenberg number Wi. **(b)** Dependence of the rms of the fluctuations of the vorticity averaged over the entire field $\langle\omega_z^{rms}\rangle_r$ on the Weissenberg number Wi. **(c)** Dependence of the local Weissenberg number Wi_{loc} on the integral Weissenberg number. The measurements were performed in isothermal conditions at the room temperature T_0.

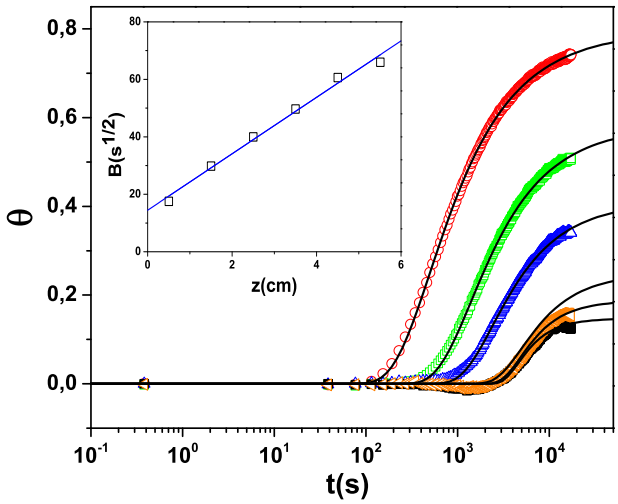

Figure 7: Time series of the reduced temperature measured with the sucrose solvent at $Re \approx 125$: circle (○) - T_1, square (□) - T_2, up triangle (△) - T_3, down triangle (▽) - T_4, left triangle (◁) - T_5, hexagon (⬡) - T_6. All measurements were performed at a distance $r = R_c/2$ from the symmetry axis of the flow container **FC**. The full lines are nonlinear fitting functions (see explanation in the text). The dependence of the fit parameter B (see text for explanation) on the vertical coordinate is presented in the insert.

strongly correlated over space and its characteristic correlation length is comparable to the radius R_c of the fluid container **FC**, [8, 7].

As the vorticity ω_z is the main quantity responsible for the heat transfer along the vertical direction z, we focus in Fig. 6 on its statistics assessed for various Weissenberg numbers spanning all the flow regimes discussed above. A peak of the space-time averaged vorticity $\langle|\omega_z|\rangle_{r,t}$ is observed within the transitional flow regime prior to reaching a plateau in the fully developed elastic turbulent regime (panel (a) in Fig. 6). The transition to elastic turbulent flow states is accompanied by a significant increase of the rms of the vorticity fluctuations (panel (b) in Fig. 6).

The measurement of space average of the rms of the vorticity allow one to calculate the local Weissenberg number as $Wi_{loc} = \lambda \left\langle \omega_z^{rms} \right\rangle_r$, Fig. 6(c). According to Liu and Steinberg, Wi_{loc} is the correct control parameter to characterise the transition to elastic turbulence as it is directly related to the polymer contribution to the stress tensor and the statistics of stretching of the polymer molecules in the flow, [28].

The main flow features illustrated in this section are consistent with previous experimental results [9, 4] and recommend the elastic turbulence as a potential candidate to efficiently transport the heat within the von Karman flow.

The following section is dedicated to a quantitative assessment of this assertion.

3.2. Heat transfer during the laminar flow of the pure solvent

Prior to investigating the heat transfer process in a regime of elastic turbulence, we focus on the heat transfer within the flow of the sucrose solvent at $Re \approx 125$ which is significantly larger than the largest Re number investigated during the experiments with the polymer solution.

Transient measurements of the reduced temperature $\theta = \frac{T_0 - T}{T_0 - T_b}$ performed at various vertical positions z and $r = R_c/2$ are presented in Fig. 7.

Each transient data set may be formally [1] fitted by $\theta = A \cdot erfc\left(\frac{B}{\sqrt{t}}\right)^C$ (the full lines in Fig. 7) where $erfc$ is the complementary error function, the parameter A describes the equilibrium temperature and $B = \frac{z}{(4\kappa)^{1/2}}$ describes the local intensity of the heat transfer process. By fitting linearly the values obtained for the coefficient B against the

[1] This functional dependence with $C = 1$ is an exact solution for the $1-D$ transient heat transfer problem only in the case of a semi-infinite planar domain with a constant temperature boundary condition. Deviations from the analytically exact result related to finite size effects may be accounted for by letting C vary as an extra fit parameter.

positions z of the thermocouples (see the insert in Fig. 7) one obtains for the thermal diffusivity of the sucrose solvent $\kappa_s \approx 2.6 \cdot 10^{-7}\ m^2 s^{-1}\ (\pm 2.3 \cdot 10^{-8}\ m^2 s^{-1})$. To compare this value with estimates based on the existing literature one can use for the thermal conductivity the value $\lambda = 0.615 W/m\ K$ reported in Ref. [33] and for the heat capacity the value $c_p = 2.5 kJ/kgK$ reported in Ref. [19]. Based on this one can estimate $\kappa_s \approx 2.238 \cdot 10^{-7}\ m^2 s^{-1}$ which is in a fair agreement with the value we have obtained above.

The equilibrium reduced temperatures reached by each thermocouple are strongly dependent on the vertical coordinate z indicating that no efficient mixing occurs in the flow which is consistent with the laminar and linear flow behaviour illustrated via measurements of the statistics of the injected power in Fig. 3. In addition to that, no fluctuations of the reduced temperature can be noted in Fig. 7 which is once more consistent with a laminar flow behaviour.

To conclude, the tests performed with the Newtonian sucrose solvent alone at the largest Reynolds number explored through the experiments with the polymer solution revealed a conductive like heat transport mechanism characterised by a strong spatial dependence of the equilibrium temperatures and a lack of temperature fluctuations. This finding corroborates well with the conclusion drawn in the first part of Sec. 3.1 regarding the lack of any significant destabilising inertial contribution to the flow.

3.3. Heat transfer in a regime of elastic turbulence

Measurements of the time series of the reduced temperature θ performed within each flow regime are presented in Fig. 8. The horizontal axis is normalised by the characteristic diffusion time t_d estimated in Sec. 2.2.

Due to the presence of the secondary flow, one can no longer resort to the complimentary error function nonlinear fit used in the case of the pure solvent in Sec. 3.2. On the other hand it can be noted that regardless the value of the Weissenberg number and the measuring position each reduced temperature time series exhibits a logarithmic scaling part (note that the data is plotted in lin-log coordinates) $\theta_r \propto a + b \cdot ln(t/t_d)$ before reaching a steady state plateau corresponding to $t/t_d \approx 1$.

The six data sets acquired within the laminar regime at $Wi = 0.8$ never collapse indicating that a temperature gradient along the vertical direction z exists at all times, Fig. 8(a). Secondly, the local slope b of the log scaling part of the reduced temperature series decreases monotonically from the bottom plate (the data set marked by a circle) to the top plate of the fluid container. This indicates that the intensity of the heat transfer is strongly inhomogeneous along the vertical direction and it is the highest near the heat sink (the bottom plate) which is what one would expect in the case of a conduction dominated heat transfer regime. Prior to entering the logarithmic scaling regime, the time series of the reduced temperature pass through a local minimum $\theta^{min} < 0$. The magnitude of this minimum decreases as one moves from the top part of the fluid container to its cooled bottom and it practically disappears at the level of the thermocouple T_1. We interpret this effect in terms of local viscous heating of the polymer solution.

The reduced temperature time series acquired within the transitional regime ($Wi = 7.7$) are presented in Fig. 8(b). As compared to the laminar case, several differences may be noted. First, within the logarithmic scaling range, the separation between the measurements performed at the six vertical positions is much smaller and so are the differences in the plateaus observed around $t \approx t_d$. This is an indication that the unsteady vortical flow observed within the transitional regime (see Fig. 5) homogenises the vertical distribution of the temperature more efficiently than the steady laminar vortex. Second, one can clearly observe in Fig. 8(b) a fluctuating component of the temperature signal which is most pronounced near the the bottom plate of the flow container (the data set labeled by a circle in Fig. 8(b)). Third, the local minimum of the temperature series acquired near the top plate is more pronounced than in the laminar case and occurs earlier which corroborates with our interpretation in terms of local viscous heating.

The six temperature time series acquired within the fully developed elastic turbulent regime at $Wi = 15.4$ nearly collapse onto a single master curve which indicates a perfectly homogeneous distribution of the temperature within the system, Fig. 8(c). Together with this, an increased level of fluctuations is observed within the logarithmic scaling range. No local minimum related to viscous heating is observed which can be explained by an efficient transport of the heat from the top of the flow cell (note the viscous heating is more effective near the top driving disk **D** due to the inhomogeneous shear in a von Karman flow configuration) to the colder bottom via the randomly fluctuating spiral vortex.

For a quantitative assessment of the local intensity of the heat transfer at various Weissenberg numbers we resort to the logarithmic slope b introduced above. The dependence of the intensity factor b obtained from the data acquired at various vertical positions on the Weissenberg number Wi is presented in Fig. 9.

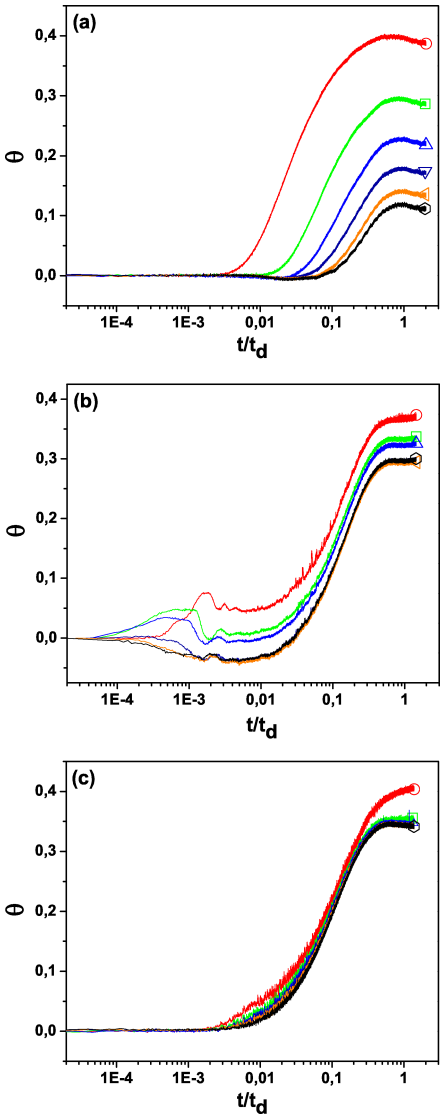

Figure 8: Time series of the reduced temperature measured at three Weissenberg numbers: **(a)** $Wi = 0.8$, **(b)** $Wi = 7.7$, **(c)** $Wi = 15.4$. The symbols in each panel refer to the vertical position of the thermocouple (see Fig. 1): circle (○) - T_1, square (□) - T_2, up triangle (△) - T_3, down triangle (▽) - T_4, left triangle (◁) - T_5, hexagon (⬡) - T_6. All measurements were performed at a distance $r = R_c/2$ from the symmetry axis of the flow container **FC**.

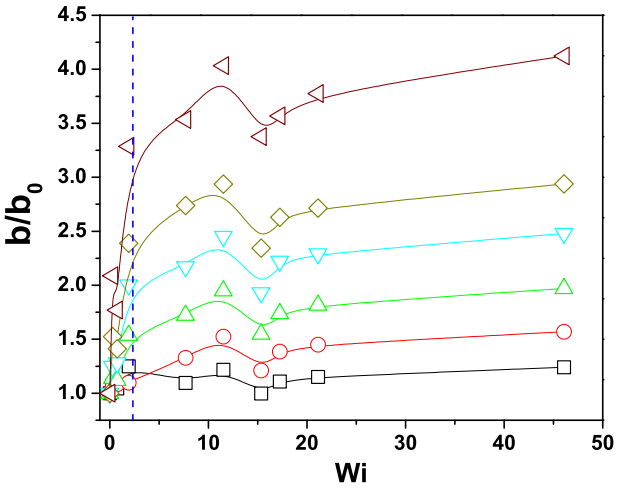

Figure 9: Dependence of the efficiency factor b obtained at various vertical positions indicated in the insert on the Weissenberg number. The symbols refer to the position along the vertical axis z (see Fig. 1): (□)- T_1, (○)- T_2, (△)- T_3, (▽)- T_4, (◇)- T_5, (◁)- T_6. The vertical dashed line indicates the onset of the primary elastic instability Wi_c.

Because the base flow does have a non-zero vertical component, an increase of the local intensity of the heat transfer related to the increase of the in plane vorticity is observed even below the onset of the primary elastic instability, $Wi = Wi_c$.

As compared to the purely conductive case, the transition to the elastic turbulence is accompanied by a roughly $3.5-4$ fold increase of the local intensity of the heat transfer at the position of the thermocouples $T_4 - T_6$. At large Wi the intensity reaches a plateau which is related to the plateau of the mean flow vorticity.

It is interesting to compare the increase in the intensity of the heat transport by elastic turbulence with similar experiments performed with Newtonian fluids at large Re in a regime of inertial turbulence. In Ref. [14] Gollub and his coworkers asses the efficiency of the heat transfer via the effective thermal diffusivity $D^* = K^*/\rho c_p$ where the global heat transport coefficient K^* is obtained from the ratio of the total measured heat flux and the local temperature gradient, ρ is the density of the fluid, and c_p is its the heat capacity. As illustrated in Fig. 2 of their paper, an increase of the efficiency of up to a factor of ten is observed at $Re = 6000$. The local increase in the heat transport intensity of roughly $3.5-4$ times we have measured within a regime elastic turbulence at $Wi = 15.4$ corresponds to the increase observed in Ref. [14] at $Re \approx 1600$.

It is equally interesting to compare our results with numerical simulations performed for the case of a von Karman flow of a Newtonian fluid. Corresponding to $Pr = 1$ and $Re = 2000$ the numerical simulations of Iwatsu for the von Karman swirling flow of a Newtonian fluid predict a maximal increase of the heat transport efficiency (quantified by the average Nusselt number) of roughly 9 times. Such a large increase in the local intensity of the heat transport by elastic turbulence was not observed during our experiments and a possible reason for that might be the nearly three orders of magnitude larger Prandtl numbers.

As the elastic turbulent flow field has a single relevant spatial scale set by the dimensions of the fluid container **FC** and there exists no physical equivalent of the cascade towards smaller scales observed in the inertial turbulence, a natural question to be answered is how does the intensity of the heat transfer depend on the position z in the flow.

To address this point, we plot in Fig. 10 the local intensity factor b versus the vertical position z for various Weissenberg numbers spanning the relevant flow regimes.

In the absence of a flow ($Wi = 0$) when the heat is transported solely by thermal conduction, a strong spatial dependence of the intensity factor is observed (the rhombs in Fig. 10). As expected for a purely conductive case, the intensity of the heat transport decreases monotonically as one moves away from the heat sink located at $z = 0$ cm.

A slight increase of the local intensity factor is observed within the laminar and steady flow regime ($Wi = 0.8$), particularly in the proximity of the top driving disk **D** (the squares). This slight increase in the intensity of the heat transfer process may be explained by the presence of the steady Ekman vortex induced by the array of the

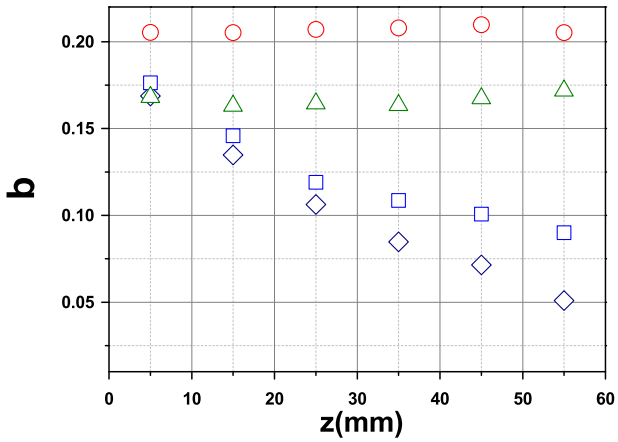

Figure 10: Dependence of the intensity factor b on the vertical coordinate. The symbols refer to the Weissenberg number: rhombs ($\diamond$) - $Wi = 0$, squares ($\square$) - $Wi = 0.8$, triangles ($\triangle$) - $Wi = 7.7$, circle ($\circ$) - $Wi = 15.4$.

thermocouples (Fig. 5). A notable increase of the heat transport intensity is observed at any measuring position within the transitional and the fully developed elastic turbulent regimes (the triangles and the circles). We point out that within these flow regimes the intensity is independent on the flow coordinate consistently with a full homogenisation of the temperature field. The largest increase in the local intensity is observed near the top disk **D** and accounts for nearly 4 times the intensity measured in a purely conductive state, Fig. 10.

To gain further insights into the statistics of the temperature fluctuations at various Weissenberg numbers, we extract the fluctuating part of each time series of the reduced temperature presented in Fig. 8 by subtracting from the original signal its pedestal $\mathscr{P}$ obtained via a fifth degree polynomial fit, $\theta_r(t/t_d) = \theta(t/t_d) - \mathscr{P}(t/t_d)$.

As by in situ measurements of the apparent viscosity η_a of the polymer solution during the heat transfer process we have observed that at high Weissenberg numbers the mechanical degradation occurs (manifested through a significant decrease of η_a) at very late stages of the process ($t/t_d > 0.5$), the whole statistical analysis we present below was restricted to time windows within the logarithmic scaling range, $0.1 < t/t_d < 0.3$ and no conclusions were drawn from the temperature data acquired beyond this range.

In the absence of a flow ($Wi = 0$) the pedestal of the signal characterises the purely conductive heat transport and in a laminar regime ($0 < Wi < Wi_c$) it describes the summed contributions of the conduction and the laminar convective transport carried on by the stable vortex illustrated in Fig. 5.

Several time series of the fluctuating part of the reduced temperature θ_r obtained according to the procedure described above from the raw data acquired by the thermocouple T_4 positioned at $r = R_c/2$ (see Fig. 1) at various Weissenberg numbers increasing from the top to the bottom are presented in Fig. 11.

In the absence of a flow ($Wi = 0$) and below the onset of the primary elastic instability ($Wi = 0.8$) these fluctuations are of a purely instrumental nature. Upon an increase of the Weissenberg number within the fully developed elastic turbulent regime a significant increase of the level of fluctuations beyond the instrumental level is observed, Fig. 11 (c,d). At $Wi = 15.4$ the randomly fluctuating temperature time series also exhibits some intermittency.

The spatial distribution of the root mean squared of the fluctuations of the reduced temperature within each flow regime is illustrated in Fig. 12.

In the absence of a flow and within the laminar regime, no dependence of the level of the fluctuations on the vertical coordinate z can be observed (which was expected, as the six thermocouples are identical, i.e. the instrumental error of their measurements is the same). Within the transitional regime and the fully developed elastic turbulent regime a clear spatial dependence of the temperature fluctuations can be observed (the triangles and the squares in Fig. 12). Due to the particular topology of the randomly fluctuating spiral vortex illustrated in Fig. 5 at $Wi = 15.4$, the fluctuations are the largest in the vicinity of the bottom plate of the flow container **FC** and decrease monotonically as one approaches the level of the top driving disk **D**. Near the bottom plate, the temperature fluctuations due to the advection of the temperature field by the random flow field are about 3.5 times larger than the instrumental fluctuations observed in the laminar regime. We point out that in spite of the clear anisotropy of the temperature fluctuations within the fully

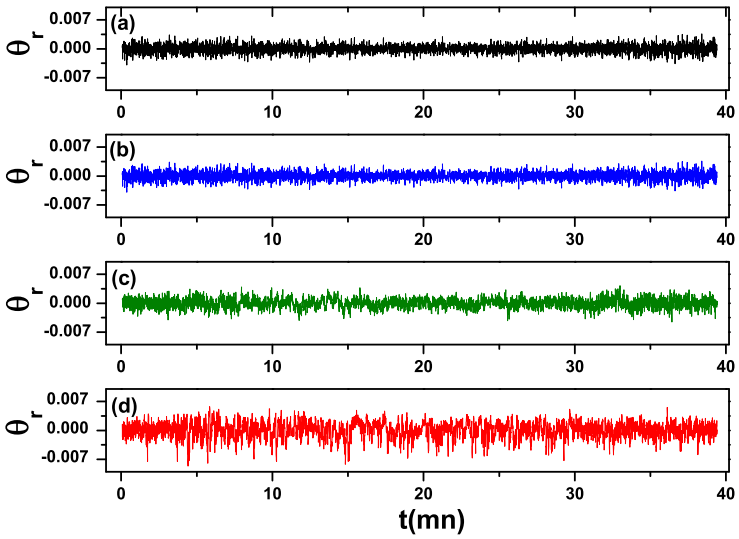

Figure 11: Time series of the fluctuating part of the reduced temperature θ_r obtained from the measurements of the thermocouple T_4 (see Fig. 1) at various Weissenberg numbers: **(a)** $Wi = 0$ **(b)** $Wi = 0.8$, **(c)** $Wi = 7.7$, **(d)** $Wi = 15.4$.

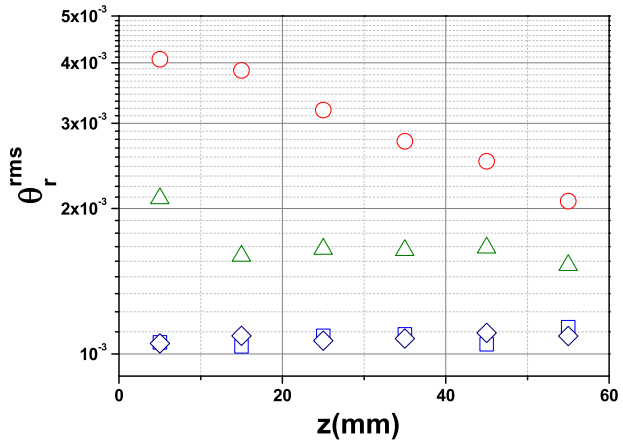

Figure 12: Space distribution of the rms of the fluctuations of the reduced temperature, θ_r^{rms} measured by the thermocouple T_4 at various Weissenberg numbers: rhombs (⋄) - $Wi = 0$, squares (□) - $Wi = 0.8$, triangles (△) - $Wi = 7.7$, circle (○) - $Wi = 15.4$.

developed elastic turbulent regime, the intensity of the heat transport quantified by the parameter b introduced above is practically independent on the spatial coordinate (the circles in Fig. 10).

The dependence of the level of fluctuations measured in the fully developed elastic turbulent regime near the bottom plate of the fluid container on the vertical coordinate indicates the possible existence of a boundary layer for the heat transfer with its edge roughly located around $z = 15$ mm, Fig. 10. As the spatial resolution of our measuring technique along the vertical direction is limited and the construction of the experimental apparatus does not allow one to move the thermocouples along this direction, a systematic investigation of this fact similar to that performed for the velocity boundary layer presented in Ref. [9] or the passive scalar boundary layer presented in Ref. [6] was not possible and should to be addressed by future experimental studies.

The probability density functions (pdf's) of the fluctuations of the reduced temperature measured by the thermocouple T_4 are presented in Fig. 13(a). In the absence of a flow (the rhombs) and within a laminar flow regime (the squares) the pdf's can be fitted by a Gaussian function (the full line).

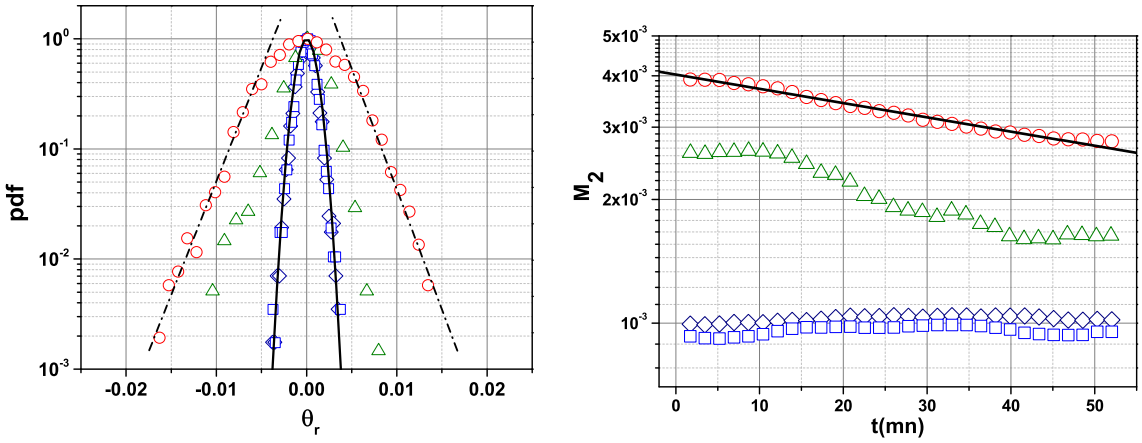

(a) (b)

Figure 13: (a) Probability density functions (pdf's) of the fluctuations of the reduced temperature, T_r^{rms}, obtained from the measurements of the thermocouple T_4. The full line is a Gaussian fit, the dash-dotted lines are guides for eye highlighting the exponential tails of the pdf's. (b) Time dependence of the second order moment M_2 of the distribution of the temperature fluctuations obtained from the measurements of the thermocouple T_4. The full line is an exponential decay fit, $M_2 \propto e^{-t/7523}$. In both panels, the symbols refer to different Wi: rhombs (◇) - $Wi = 0$, squares (□) - $Wi = 0.8$, triangles (△) - $Wi = 7.7$, circles (○) - $Wi = 15.4$.

Upon an increase of the Weissenberg number beyond the onset of the primary elastic instability (the triangles and the circles) the distributions become significantly broader and exhibit exponential tails (see the dash-dot lines).

A certain degree of asymmetry of the pdf's which may be associated to the intermittency of the temperature fluctuations visible in Fig. 11(c-d) can be equally observed.

The decay of the second order moments M_2 of the probability density functions is illustrated in Fig. 13(b). Within the elastic turbulent regime (the circles) an exponential decay of the second order moment is observed, $M_2 \propto e^{-t/t_{mix}}$. Here t_{mix} is a characteristic time scale for the decay of the temperature fluctuations and is equivalent to the mixing time in the passive scalar problem. By an exponential fit of the data presented in Fig. 13(b) one obtains $t_{mix} \approx 7523$ s which is about 3.4 times smaller than the characteristic time diffusion time t_d. This result corroborates with the 3.5 times increase in the efficiency of the heat transfer quantified by the slope b and illustrated in Figs. 9, 10.

The pdf's of the fluctuations of the reduced temperature measured at each vertical position for various Wi are presented in Fig. 14. In the absence of a flow and within the laminar regime the pdf's acquired at each of the six vertical positions collapse onto a single master curve which can be well fitted by a Gaussian distribution (panels (a-b)).

Within the transitional regime ($Wi = 7.7$) a strongly intermittent distribution is observed particularly in the vicinity of the bottom plate (the squares and the circles in panel (c)). This behaviour may be related to the peak of the time averaged vorticity visible in Fig. 6(a). The degree of intermittency decreases as one approaches the top disk but does not vanish.

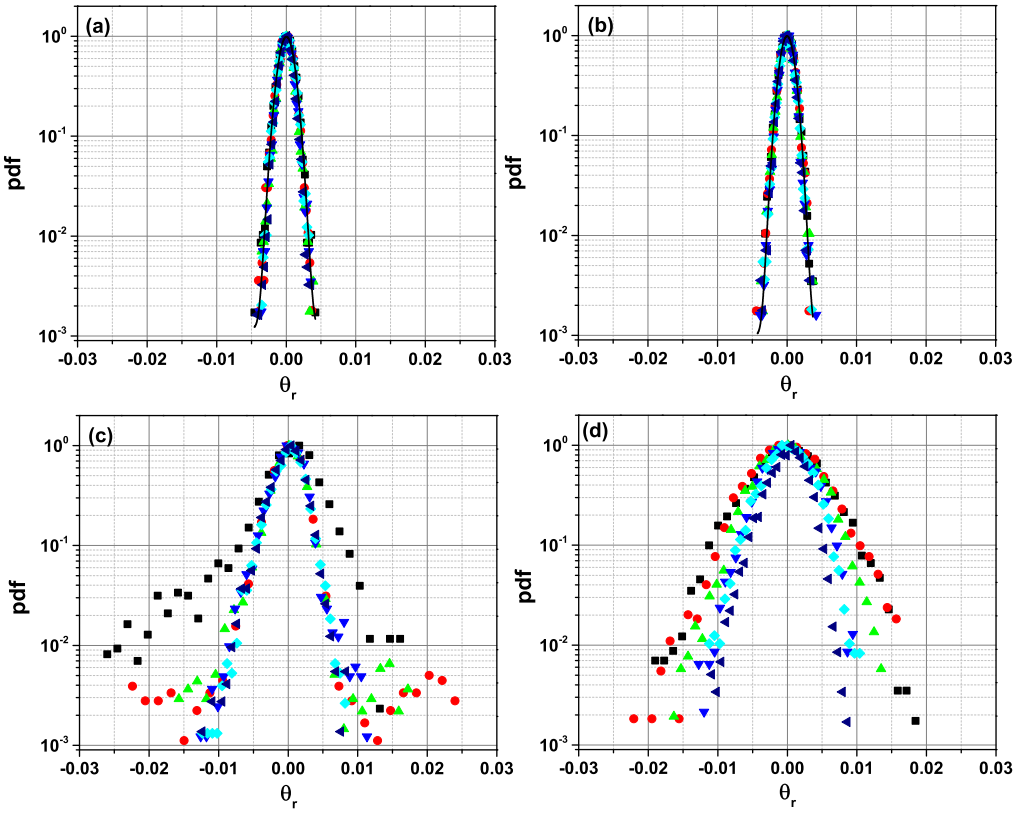

Figure 14: Pdf's of the fluctuations of the reduced temperature measured at various vertical positions and several Wi: **(a)** $Wi = 0$ **(b)** $Wi = 0.8$ **(c)** $Wi = 7.7$ **(d)** $Wi = 15.4$. In each panel the symbols refer to different thermocouples (see Fig. 1): squares (■) - T_1, circles (●) - T_2, up triangles (▲) - T_3, down triangles (▼) - T_4, rhombs (◆) - T_5, left triangles (◀) - T_6. The full lines in panels (a,b) are Gaussian fitting functions.

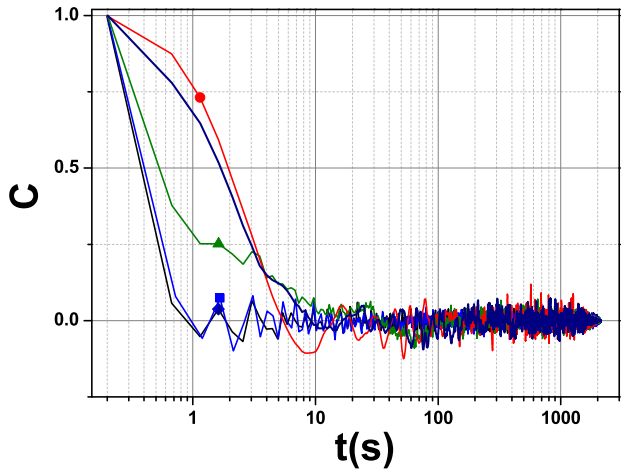

Figure 15: Temporal autocorrelation functions C of the fluctuations of the reduced temperature measured measured by the thermocouple T_4 at various Weissenberg numbers: rhombs (◆) - $Wi = 0$, squares (■) - $Wi = 0.8$, triangles (▲) - $Wi = 7.7$, circles (●) - $Wi = 15.4$.

In the fully developed elastic turbulent regime the pdf's exhibit an intermittent behaviour and exponential tails regardless the vertical position, panel (d).

These results on the statistics of the fluctuations of the reduced temperature presented above are in a good agreement with the theoretical prediction for the decay of a passive scalar in a random smooth flow, [11, 2], and with the experiments on the mixing of a passive scalar in a macroscopic curvilinear channel, [16], and in a micro channel, [5, 6].

The temporal auto-correlation functions of the fluctuations of the reduced temperature measured within each relevant flow regime are presented in Fig. 15.

In the absence of a flow and within the laminar regime the fluctuations of the reduced temperature are solely related to the instrumental noise of the temperature measurements and, consequently, the signals are short correlated (the curves labeled by a rhomb and a square in Fig. 15). Within the transitional and the fully developed elastic turbulent regimes the reduced temperature de-correlates over characteristic times τ_c comparable to the relaxation time of the polymer λ. This behaviour is quite similar to the behaviour of the time autocorrelation functions of the azimuthal velocity component, see Fig. 24 in Ref. [9] which is probably due to the coupling between the flow field and the temperature field.

Although a logarithmic decay of the time autocorrelation is apparent in the elastic turbulent regime (see the linear decay part of the curve labeled by a circle in Fig. 15 and note that the horizontal axis is plotted over a log scale), a systematic comparison with the theoretical prediction for the decay of spatial autocorrelations of a passive scalar [11, 2] is not straightforward. The main limitation comes from the usage of the Taylor frozen flow hypothesis that would allow the conversion of the time autocorrelations into space autocorrelations. First, with the present apparatus, we do not have access to the vertical flow component but only measure the in plane velocity fields. Second, even if one could measure the vertical velocity component, it has been demonstrated that due to the strong spatial coherence of the flow fields, the applicability of the Taylor hypothesis is limited in the case of the elastic turbulence, [8]. The study of the spatial correlations of the temperature field requires the implementation of a different measuring technique able to capture directly the spatial distribution of the temperature within the flow.

The spectra of the fluctuations of the reduced temperature θ_r are presented in Fig. 16. Both in the absence of a flow ($Wi = 0$) and within a laminar regime ($Wi = 0.8$) the power spectrum is flat over the entire frequency range and it corresponds to the level of the instrumental noise of the thermocouples.

A gradual increase of the Weissenberg number towards the fully developed elastic turbulent regime reveals a power law decay of the spectrum $P \propto f^{-1.1}$ which, towards the upper bound of the frequency range, falls onto the same instrumental noise plateau.

This behaviour is equally similar to that observed in the decay of a passive scalar in a smooth random flow.

The similarities of the statistics of the temperature fluctuations with that of a passive scalar convected by a random

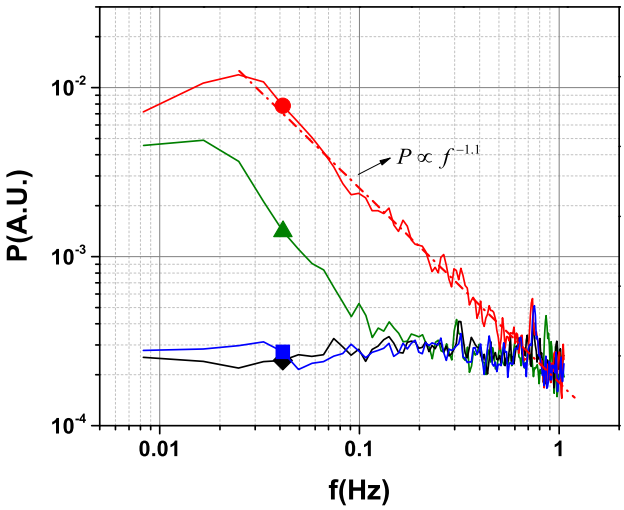

Figure 16: Spectra of the fluctuations of the reduced temperature θ_r measured by the thermocouple T_4 (see Fig. 1) at various Weissenberg numbers: rhombs (◆) - $Wi = 0$, squares (■) - $Wi = 0.8$, triangles (▲) - $Wi = 7.7$, circle (●) - $Wi = 15.4$. The dash - dot line is a guide for the eye, $P \propto f^{-1.1}$.

smooth flow prompts us to investigate closer the passive/active character of the heat transport process. This concern is motivated by the fact that local changes in the flow temperature result in changes of the polymer relaxation time which in turn may induce local changes in the structure of the flow due to the strong spatial inhomogeneity of the elastic stress.

To address this point, a comparative analysis of the time averaged flow patterns measured at three different stages of the heat transfer process is presented in Fig. 17.

Within the transitional flow regime at $Wi = 7.7$ (the top row in Fig. 17), the heat transfer process induces no visible changes in either the topology of the time averaged flow pattern or the magnitude of the mean flow speed. Each of the flow patterns acquired at various stages of the cooling t/t_d reproduces quite faithfully the flow pattern acquired at the same Weissenberg number in isothermal conditions, Fig. 5. A similar conclusion can be drawn within the fully developed turbulent regime $Wi = 15.4$ (the bottom row in Fig. 17) except for the flow pattern acquired at late stages of cooling $t/t_d = 0.56$ where a slight increase of the mean flow speed may be noticed. We attribute this to the mechanical degradation of the polymer chains which translates into a decrease of the apparent viscosity η_a of the polymer solution. However, we point out once again that the statistical analysis presented above used only the temperature data acquired within the decay regime $t/t_d < 0.2$ (see panel (c) in Fig. 8) when no mechanical degradation was observed (the apparent viscosity η_a did not diminish in time).

The overall conclusion of this comparative assessment of the flow patterns at various stages of the heat transport process is that, in this case, the temperature field behaves as a passive scalar field which explains several similarities in the statistics of the temperature fluctuations with the case of mixing of a low diffusivity tracer, [6, 5].

4. Conclusions, outlook

An experimental study of the efficiency of the heat transfer process in a regime of elastic turbulence was presented. The transition towards elastic turbulence via a primary elastic instability has been described in Sec. 3.1 by both integral measurements of the statistics of the injected power and by local and time resolved characterisation of the flow fields using the **DPIV** technique.

Preliminary tests performed with the solvent alone within the same range of Reynolds numbers explored with the polymer solution revealed no increase in either the flow resistance or the fluctuations of the global power injected into the flow. Consequently, a conductive like heat transport characterised by a strong vertical gradient of the equilibrium temperatures and lack of fluctuations of the local temperature time series is observed. Based on these tests, one can rule out any possible inertial contributions to the flow during the tests performed with the viscoelastic fluid.

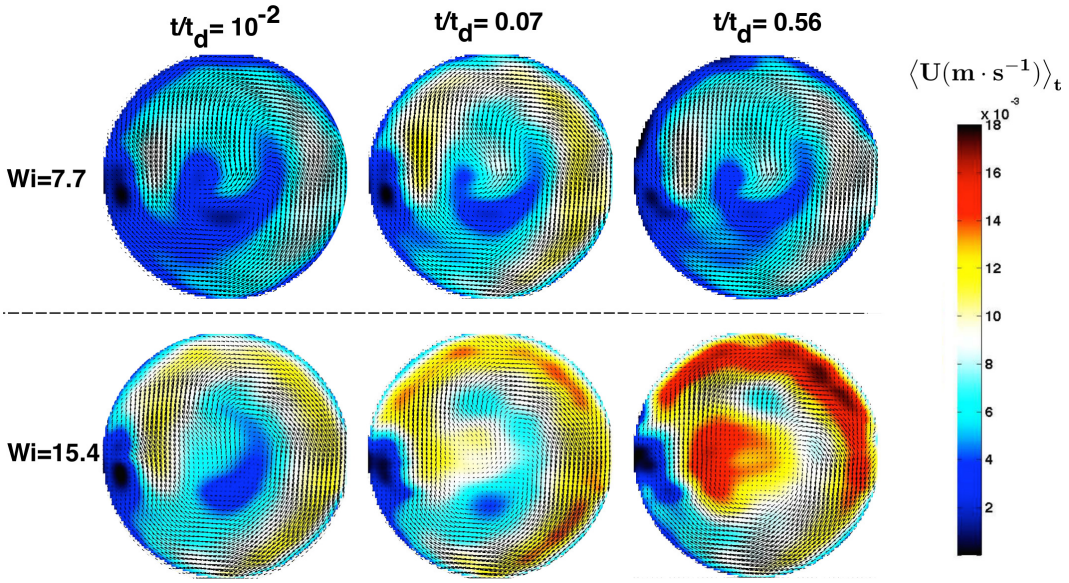

Figure 17: Time averaged flow patterns at various stages t/t_d of the heat transfer process measured at $Wi = 7.7$ (top row) and $Wi = 15.4$ (bottom row). The colour maps refer to the absolute value of the flow velocity. For the clarity of the presentation, the overlapped vector fields were down-sampled by a factor of 2 along each direction.

The characterisation of the transition to elastic turbulence and of the elastic turbulent flows presented in Sec. 3.1 reveals several flow features already established by previous experimental studies concerning the viscoelastic von Karman swirling flow, [4, 9, 17].

At an integral scale, the transition to elastic turbulence is accompanied by a significant increase of the mean injected power beyond its laminar values, Fig. 4(a), and of its level of fluctuations, Fig. 4(b). The increase of the flow resistance observed at an integral scale is due to a major reorganisation of the flow field past the onset of the primary elastic instability and within the fully developed elastic turbulent regime, Fig. 5.

Although the topology of the laminar flow field is different from that described in Refs. [4, 9] due to the presence of the thermocouples which induce a stationary Ekman vortex even below the onset of the elastic instability Wi_c, several main features of the transitional and the fully developed turbulent regimes are faithfully recovered at $Wi > Wi_c$: randomly fluctuating velocity fields, high spatial correlation of the flow fields over a characteristic length comparable to the radius of the fluid container. Together with this, a significant increase of both the vorticity and its rms of fluctuations is observed past the onset of the elastic instability, Fig. 6.

The effect of the random flow on the efficiency of the heat transfer process is studied in Sec. 3.3. Point-wise measurements of the logarithmic rate of change of the temperature assessed via the parameter b performed at various Weissenberg numbers indicate that the transition to elastic turbulence is accompanied by an increased efficiency of the heat transfer, Fig. 9. As compared to the laminar flow state, the increase in the efficiency can be as large as four fold (in the vicinity of the top driving disk). Within the elastic turbulent regime the individual time series of the normalised temperature θ acquired at various vertical positions z collapse onto a single master curve Fig. 8 and, consequently, the intensity of the heat transfer is independent on the vertical coordinate, Fig. 10. This demonstrates the ability of the elastic turbulent flow to homogenise the temperature distribution over the entire fluid volume.

The increase in the intensity of the heat transfer is related to the increase of the in-plane vorticity and of its rms of fluctuations which translates into strong fluctuations of the temperature time series, Fig. 11. Unlike the efficiency factor b, the rms of the reduced temperature fluctuations measured with the elastic turbulence regime is strongly inhomogeneous along the vertical direction, Fig. 12. The level of fluctuations is the largest in the vicinity of the bottom plate of the fluid container **FC** and decreases monotonically towards the top disc.

The analysis of the statistics of the temperature fluctuations within the elastic turbulent regime reveals several features that are similar to the problem of the decay of a passive scalar in a random smooth flow:

1. exponential tails of the probability distribution functions, Fig. 13(a).
2. exponential decay of the second order moment of the probability distribution, Fig. 13(b).
3. time autocorrelations that decay over characteristic times comparable to the correlation time of the flow and the characteristic relaxation time of the polymer, Fig. 15.
4. power law decay of the power spectrum of the temperature fluctuations $P \approx f^{-\delta}$ with $\delta \approx 1.1$, Fig. 16.

The similarity of the heat transfer scenario with the passive scalar problem is further reinforced by a comparative analysis of isothermal and non-isothermal flow patterns, Fig. 17.

To conclude, although the dependence of the polymer relaxation time on the temperature could in principle alter the passive scalar heat transfer scenario typically expected in the absence of buoyancy terms, no significant effect of the cooling on the flow topology was observed confirming the passive evolution of the temperature field.

The increase in the heat transfer intensity due to the elastic turbulent flow is comparable in magnitude to the increase observed in an inertial turbulent flow at $Re \approx 1600$, [14, 24]. This quantitative comparison recommends the elastic turbulence as a viable heat transport alternative in situations when the inertial turbulence is unpractical such as microscopic flows.

It is instructive to compare the relative increase of the intensity of the heat transfer by elastic turbulence with the relative increase of the efficiency of the mixing of a passive scalar by elastic turbulence in a similar von Karman swirling flow. The relative (to the molecular diffusion) increase of the efficiency of the mixing of a passive scalar with a diffusion coefficient $D \approx 5.5 \cdot 10^{-10} cm^2/s$ observed in Ref. [9] was significantly larger than the relative (to the heat conduction) increase in the efficiency observed in the case of heat transport we have studied through this paper. To understand this apparent discrepancy, we will simplistically assess the relative increase in the transport efficiency via a ratio of the time scales associated to each transfer mechanism: $\frac{t_D}{t_f}$ in the case of the mixing and $\frac{t_d}{t_f}$ in the case of the heat transfer. Here $t_D = H^2/D$ is the characteristic time associated to the molecular diffusion, t_d is the characteristic time associated to the thermal conduction already defined in Sec. 2.2 as $t_d = H^2/\kappa$ and t_f a characteristic time associate to the random flow which, for simplicity, can be estimated as the inverse vorticity, $t_f \approx \omega_z^{-1}$. Now, bearing in mind that numerically $D \ll \kappa$ (the difference accounts for several orders of magnitude), one can readily conclude $\frac{t_D}{t_f} \gg \frac{t_d}{t_f}$ which explains why the relative increase of the transport efficiency is significantly larger in the passive scalar case.

This experimental study leaves open several questions that could make the object of future experimental investigations.

The first one concerns with a detailed analysis of the three dimensional spatial structure of the temperature field and its relation to three dimensional flow structure which is already well documented, [4, 9]. Such an analysis should be able to probe the existence of a heat transfer boundary layer as well as the scaling of its widths with the relevant flow/thermal parameters.

A second fundamental question related to the temperature dependence of both the solution's viscosity and the largest relaxation time is whether the similarity of the heat transfer with the decay of the passive scalar would remain unaltered upon an increase of temperature range.

Last, from a practical standpoint it would be interesting to employ the elastic turbulence in efficiently transporting the heat in curvilinear open channels.

5. Acknowledgments

We thank Professor Victor Steinberg for a critical reading of our manuscript and valuable suggestions which helped improving the manuscript.

Gwenaël Biotteau is gratefully acknowledged for designing and machining the experimental apparatus. We are indebted to Christophe Le Bozec for his help in setting up the data acquisition protocol.

We gratefully acknowledge the financial support from the *Agence Nationale de la Recherche* (ANR) via the project HoTeT.

[1] Aref, H., 1990. Chaotic advection of fluid particles. Philosophical Transactions of the Royal Society of London. Series A: Physical and Engineering Sciences 333 (1631), 273–288.
URL http://rsta.royalsocietypublishing.org/content/333/1631/273.abstract

[2] Balkovsky, E., Fouxon, A., Oct 1999. Universal long-time properties of lagrangian statistics in the batchelor regime and their application to the passive scalar problem. Phys. Rev. E 60, 4164–4174.
URL http://link.aps.org/doi/10.1103/PhysRevE.60.4164
[3] Bird, B. R., Hassager, O., May 1987. Dynamics of Polymeric Liquids, Fluid Mechanics (Dynamics of Polymer Liquids Vol. 1), 2nd Edition. Vol. 1. Wiley-Interscience.
[4] Burghelea, T., 2005. Elastic turbulence and mixing in a dilute polymer solution. Ph.D. thesis, Feinberg Graduate School of the Weizmann Iinstitute of Science.
[5] Burghelea, T., Segre, E., Bar-Joseph, I., Groisman, A., Steinberg, V., Jun 2004. Chaotic flow and efficient mixing in a microchannel with a polymer solution. Phys. Rev. E 69, 066305.
URL http://link.aps.org/doi/10.1103/PhysRevE.69.066305
[6] Burghelea, T., Segre, E., Steinberg, V., Apr 2004. Mixing by polymers: Experimental test of decay regime of mixing. Phys. Rev. Lett. 92, 164501.
URL http://link.aps.org/doi/10.1103/PhysRevLett.92.164501
[7] Burghelea, T., Segre, E., Steinberg, V., 2004. Statistics of particle pair separations in the elastic turbulent flow of a dilute polymer solution. EPL (Europhysics Letters) 68 (4), 529.
URL http://stacks.iop.org/0295-5075/68/i=4/a=529
[8] Burghelea, T., Segre, E., Steinberg, V., 2005. Validity of the Taylor hypothesis in a random spatially smooth flow. Physics of Fluids 17 (10), 103101–1, 103101–8.
URL http://scitation.aip.org/content/aip/journal/pof2/17/10/10.1063/1.2077367
[9] Burghelea, T., Segre, E., Steinberg, V., 2007. Elastic turbulence in von Karman swirling flow between two disks. Physics of Fluids (1994-present) 19 (5), –.
URL http://scitation.aip.org/content/aip/journal/pof2/19/5/10.1063/1.2732234
[10] Celani, A., Cencini, M., Mazzino, A., Vergassola, M., Nov 2002. Active versus passive scalar turbulence. Phys. Rev. Lett. 89, 234502.
URL http://link.aps.org/doi/10.1103/PhysRevLett.89.234502
[11] Chertkov, M., Falkovich, G., Kolokolov, I., Lebedev, V., Jun 1995. Statistics of a passive scalar advected by a large-scale two-dimensional velocity field: Analytic solution. Phys. Rev. E 51, 5609–5627.
URL http://link.aps.org/doi/10.1103/PhysRevE.51.5609
[12] Ekman, V. W., 1905. On the influence of the earth's rotation on ocean currents. Ark. Mat, Astron. Fys. 2 (11), 1 – 53.
[13] El Omari, K., Le Guer, Y., 2010. Thermal chaotic mixing of power-law fluids in a mixer with alternately rotating walls. Journal of Non-Newtonian Fluid Mechanics 165 (1112), 641 – 651.
URL http://www.sciencedirect.com/science/article/pii/S037702571000090X
[14] Gollub, J. P., Clarke, J., Gharib, M., Lane, B., Mesquita, O. N., Dec 1991. Fluctuations and transport in a stirred fluid with a mean gradient. Phys. Rev. Lett. 67, 3507–3510.
URL http://link.aps.org/doi/10.1103/PhysRevLett.67.3507
[15] Groisman, A., Steinberg, V., 2000. Elastic turbulence in a polymer solution flow. Nature 405 (6782), 53–55.
[16] Groisman, A., Steinberg, V., 2001. Efficient mixing at low reynolds numbers using polymer additives. Nature 410 (6831), 905–908.
[17] Groisman, A., Steinberg, V., Jan 2001. Stretching of polymers in a random three-dimensional flow. Phys. Rev. Lett. 86, 934–937.
URL http://link.aps.org/doi/10.1103/PhysRevLett.86.934
[18] Groot, J. D., Kestin, J., Sookiazian, H., 1974. Instrument to measure the thermal conductivity of gases. Physica 75 (3), 454 – 482.
URL http://www.sciencedirect.com/science/article/pii/0031891474903413
[19] Gucker, F. T., Ayres, F. D., 1937. The specific heats of aqueous sucrose solutions at 20 and 25 and the apparent molal heat capacity of non-electrolytes1. Journal of the American Chemical Society 59 (3), 447–452.
[20] Healy, J., de Groot, J., Kestin, J., 1976. The theory of the transient hot-wire method for measuring thermal conductivity. Physica B+C 82 (2), 392 – 408.
URL http://www.sciencedirect.com/science/article/pii/0378436376902035
[21] Hobbs, D., Muzzio, F., 1997. The kenics static mixer: a three-dimensional chaotic flow. Chemical Engineering Journal 67 (3), 153 – 166.
URL http://www.sciencedirect.com/science/article/pii/S1385894797000132
[22] Iwatsu, R., 2004. Flow pattern and heat transfer of swirling flows in cylindrical container with rotating top and stable temperature gradient. International Journal of Heat and Mass Transfer 47 (12-13), 2755 – 2767.
URL http://www.sciencedirect.com/science/article/pii/S0017931004000171
[23] Jun, Y., Steinberg, V., 2010. Mixing of passive tracers in the decay batchelor regime of a channel flow. Physics of Fluids (1994-present) 22 (12), –.
URL http://scitation.aip.org/content/aip/journal/pof2/22/12/10.1063/1.3522400
[24] Lane, B. R., Mesquita, O. N., Meyers, S. R., Gollub, J. P., 1993. Probability distributions and thermal transport in a turbulent grid flow. Physics of Fluids A: Fluid Dynamics (1989-1993) 5 (9), 2255–2263.
URL http://scitation.aip.org/content/aip/journal/pofa/5/9/10.1063/1.858564
[25] Lee, C. H., Hyun, J. M., 1999. Flow of a stratified fluid in a cylinder with a rotating lid. International Journal of Heat and Fluid Flow 20 (1), 26 – 33.
URL http://www.sciencedirect.com/science/article/pii/S0142727X98100413
[26] Liu, Y., Jun, Y., Steinberg, V., 2007. Longest relaxation times of double-stranded and single-stranded dna. Macromolecules 40 (6), 2172–2176.
URL http://pubs.acs.org/doi/abs/10.1021/ma062715d
[27] Liu, Y., Jun, Y., Steinberg, V., 2009. Concentration dependence of the longest relaxation times of dilute and semi-dilute polymer solutions. Journal of Rheology (1978-present) 53 (5), 1069–1085.
URL http://scitation.aip.org/content/sor/journal/jor2/53/5/10.1122/1.3160734

[28] Liu, Y., Steinberg, V., 2010. Molecular sensor of elastic stress in a random flow. EPL (Europhysics Letters) 90 (4), 44002.
URL http://stacks.iop.org/0295-5075/90/i=4/a=44002
[29] Mokrani, A., Castelain, C., Peerhossaini, H., 1997. The effects of chaotic advection on heat transfer. International Journal of Heat and Mass Transfer 40 (13), 3089 – 3104.
URL http://www.sciencedirect.com/science/article/pii/S0017931096003614
[30] Mota, J. P. B., Rodrigo, A. J. S., Saatdjian, E., 2007. Optimization of heat-transfer rate into time-periodic two-dimensional stokes flows. International Journal for Numerical Methods in Fluids 53 (6), 915–931.
URL http://dx.doi.org/10.1002/fld.1312
[31] Ottino, J. M., 1989. The kinematics of mixing: Stretching, chaos, and transport. Cambridge and New York, Cambridge University Press, 1989, 375 p.
[32] Raffel, M., Willert, C. E., Wereley, S. T., Kompenhans, J., September 2007. Particle Image Velocimetry: A Practical Guide (Experimental Fluid Mechanics). Springer; 2nd edition.
[33] Riedel, L., 1949. Wärmeleitfähigkeitsmessungen an zuckerlösungen, fruchtsäften und milch. Chem. Ing. Technik 17 (18), 340 – 341.
[34] Scarano, F., Rhiethmuller, M. L., 2001. Advances in iterative multigrid piv image processing. Exp. Fluids 29.
[35] Shraiman, B., Siggia, E., JUN 8 2000. Scalar turbulence. NATURE 405 (6787), 639–646.
[36] Timité, B., Castelain, C., Peerhossaini, H., 2011. Mass transfer and mixing by pulsatile three-dimensional chaotic flow in alternating curved pipes. International Journal of Heat and Mass Transfer 54 (1718), 3933 – 3950.
URL http://www.sciencedirect.com/science/article/pii/S001793101100250X
[37] Tirtaatmadja, V., Sridhar, T., 1993. A filament stretching device for measurement of extensional viscosity. Journal of Rheology (1978-present) 37 (6), 1081–1102.
URL http://scitation.aip.org/content/sor/journal/jor2/37/6/10.1122/1.550372
[38] Titon, J. H., Cadot, O., 2003. The statistics of power injected in a closed turbulent flow: Constant torque forcing versus constant velocity forcing. Physics of Fluids (1994-present) 15 (3), 625–640.
URL http://scitation.aip.org/content/aip/journal/pof2/15/3/10.1063/1.1539856
[39] Toussaint, V., Carriere, P., Raynal, F., NOV 1995. A numerical Eulerian approach to mixing by chaotic advaection. Physics of fluids 7 (11), 2587–2600.
[40] Toussaint, V., Carriere, P., Scott, J., Gence, J., NOV 2000. Spectral decay of a passive scalar in chaotic mixing. PHYSICS OF FLUIDS 12 (11), 2834–2844.
[41] Warhaft, Z., 2000. Passive scalars in turbulent flows. Annual Review of Fluid Mechanics 32 (1), 203–240.
URL http://dx.doi.org/10.1146/annurev.fluid.32.1.203